# Temperature dependence of the magnon-phonon interaction in hybrids of high-overtone bulk acoustic resonators with ferromagnetic thin films

M. Müller,[1,2,*] J. Weber,[1,2] S.T.B. Goennenwein,[3] S. Viola Kusminskiy,[4,5] R. Gross,[1,2,6] M. Althammer,[1,2,†] and H. Huebl[1,2,6,‡]

[1] *Walther-Meißner-Institut, Bayerische Akademie der Wissenschaften, 85748 Garching, Germany*
[2] *TUM School of Natural Sciences, Technical University of Munich, 85748 Garching, Germany*
[3] *Department of Physics, University of Konstanz, 78457 Konstanz, Germany*
[4] *Institute for Theoretical Solid State Physics, RWTH Aachen, 52074 Aachen, Germany*
[5] *Max Planck Institute for the Science of Light, 91058 Erlangen, Germany*
[6] *Munich Center for Quantum Science and Technology (MCQST), 80799 Munich, Germany*

(Received 29 November 2023; revised 28 January 2024; accepted 5 February 2024; published 18 March 2024)

Tailored magnon-phonon hybrid systems, in which high-overtone bulk acoustic resonators couple resonantly to the Kittel mode of a ferromagnetic thin film, are considered optimal for the creation of acoustic phonons with a defined circular polarization. This class of devices is therefore ideal for the investigation of phonon-propagation properties and assessing their capacity to transport angular momentum in the classical, and potentially even in the quantum, regime. Here, we study the coupling between the magnons in a ferromagnetic $Co_{25}Fe_{75}$ thin film and the transverse acoustic phonons in bulk acoustic wave resonators formed by the sapphire substrate onto which the film is deposited. Using broadband ferromagnetic resonance experiments as a function of temperature, we investigate the strength of the coherent magnon-phonon interaction and the individual damping rates of the magnons and phonons participating in the process. This demonstrates that this coupled magnon-phonon system can reach a cooperativity $C \approx 1$ at cryogenic temperatures. Our experiments also showcase the potential of strongly coupled magnon-phonon systems for strain-sensing applications.

DOI: 10.1103/PhysRevApplied.21.034032

## I. INTRODUCTION

Spin-orbit coupling and its consequences, such as finite magnetoelastic coupling (MEC), can transduce fundamental excitations of solid-state systems between different forms. For magnetic excitations, the conversion of excitations of the spin system (magnons) to those of the lattice (phonons) typically manifests as damping of the magnetization dynamics [1–7]. On the other hand, the same MEC allows to coherently excite magnetization dynamics by elastic waves [8–17] to control the magnetization direction by elastic strain [8,9,18–21], or to generate perpendicular magnetic anisotropy [8,22–25]. Thus, the magnetoelastic interaction, with its potential to couple magnons and phonons, is considered as a route toward strong magnon-phonon coupling, which shows in the form of hybridized excitations [14,26–29]. Recently, the controlled magnon-phonon coupling in geometrically tailored systems or multilayer systems has been discussed as a means of studying and controlling magnetization damping via phonons [30,31], in the excitation of helical phonons [32,33], in the study of strong coupling in magnon-phonon hybrids [34,35], and in applications in quantum sensing and transduction [17,36–44]. Several seminal experiments explore bulk acoustic wave (BAW) resonators based on gadolinium gallium garnet ($Gd_3Ga_5O_{12}$, GGG) substrates carrying a heteroepitaxial ferrimagnetic yttrium iron garnet ($Y_3Fe_5O_{12}$, YIG) thin film [32,33,35]. The choice for this particular material system is mostly motivated by the exceptional magnetic damping properties of YIG [7,45–47]. However, YIG requires substrate materials that allow for heteroepitaxial growth. Moreover, YIG shows enhanced magnetization damping at cryogenic temperatures [45,46,48], where reduced acoustic losses [49,50] in combination with an increased MEC [51] potentially offer improved cooperativities $C$. In contrast, ferromagnetic metallic (FM) thin films with ultralow magnetic damping properties, such as $Co_{25}Fe_{75}$ (CoFe), allow for the creation of magnon-phonon hybrids with a broad selection of substrate materials acting as the BAW resonator [52]. Here, we report on the temperature dependence of the acoustic and magnetic damping as well as the magnetoelastic

*manuel.mueller@wmi.badw.de
†matthias.althammer@wmi.badw.de
‡hans.huebl@wmi.badw.de

 

coupling rate in FM/BAW resonator substrate bilayer systems.

In our experiments, we study the temperature and frequency evolution of the magnetic relaxation rate $\kappa_s$ and the elastic relaxation rate $\eta_a$, as well as the effective magnetoelastic coupling rate $g_{eff}$ for magnetic CoFe thin films deposited on $Al_2O_3$ BAW resonators. We find that the results for both $\kappa_s$ and $\eta_a$ can be well understood within the models of Gilbert damping in 3*d* transition metals [53–57] and Landau-Rumer theory [49,50], respectively. In addition, we investigate the temperature dependence of the magnon-phonon coupling rate $g_{eff}$ and the resulting cooperativity $C$ to identify optimal operation conditions for mode hybridization [32,33]. We also assess the potential of magnon-phonon hybrids for strain sensing.

## II. EXPERIMENTAL DETAILS

Our ferromagnet-insulator system comprises a Pt(3 nm)/Cu(3 nm)/CoFe(30 nm)/Cu(3 nm)/Ta(3 nm) multilayer stack deposited via dc magnetron sputtering on a $L = 510$ μm thick sapphire [$Al_2O_3$ (0001)] substrate, which is polished on both sides. The Pt(3 nm)/Cu(3 nm) seed layer ensures optimal magnetization-damping properties of the CoFe film, while enabling elastic coupling to the standing-wave phonons in the substrate [52,58,59]. The Cu(3 nm)/Ta(3 nm) top layer serves for corrosion protection. To analyze the magnon-phonon coupling, we perform broadband ferromagnetic resonance (FMR) experiments in a cryogenic environment. In particular, the sample is mounted face down onto a coplanar waveguide (CPW) with a width of $w = 1.39$ cm, a length of $l = 2.54$ cm and a center-conductor width of $w_{cc} \simeq 120$ μm such that the Ta top layer is facing the CPW. We measure the complex microwave transmission parameter $S_{21}$ of the CPW as a function of the frequency $\omega$ and the static applied magnetic field $H_{ext}$ using a vector network analyzer (VNA). The external static magnetic field is applied along the out-of-plane direction, resulting in the generation of standing circularly polarized elastic shear waves exhibiting the same frequency in the gigahertz range and helicity as the magnonic mode due to magnetoelastic coupling between the spin system and the lattice [32,35,52]. As the magnetic thin film is elastically coupled to the substrate serving as the BAW resonator, the joint film-substrate system can be considered as a single elastic object in which high-overtone ($n \simeq 1000$) bulk acoustic waves are excited by the magnetization dynamics in the FM layer. Here, we select the out-of-plane geometry to achieve the highest coupling rates. However, though less efficiently, elastic waves can also be excited in the in-plane geometry [30,34]. A sketch of the measurement setup and geometry is presented in Fig. 1(a).

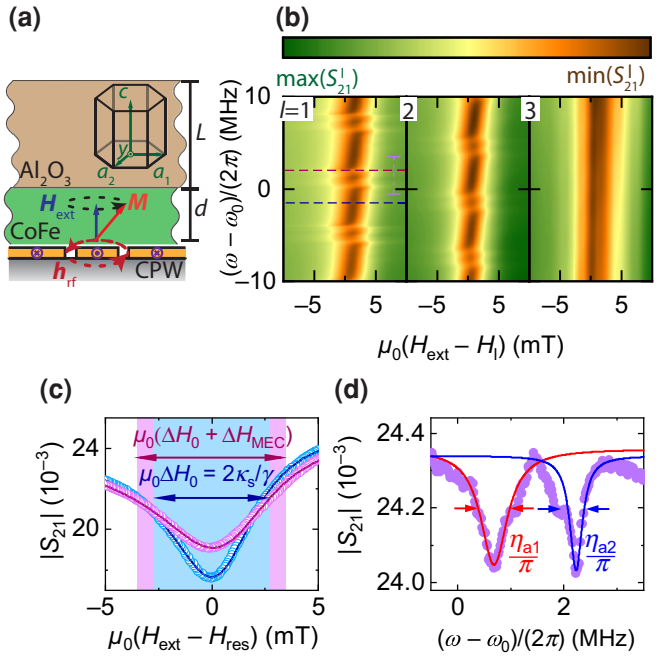


FIG. 1. (a) A sketch of the experimental configuration, with the sample mounted face to face on a coplanar waveguide. (b) The CPW microwave transmission $|S_{21}|$ plotted as a function of the frequency $\omega$ around $\omega_0/(2\pi) = 18$ GHz and the external magnetic field $H_{ext}$ close to the FMR resonance field $H_l$ for various temperatures indexed by $l$ (see Table I). (c) The fixed frequency $|S_{21}|$, showing the FMR microwave absorption on resonance (magenta) and off resonance (blue) with the $n$th bulk elastic resonance mode. The respective frequencies are indicated by dashed lines in (b). (d) $|S_{21}|$ plotted versus the frequency for a fixed magnetic field detuned from the FMR resonance field [see the vertical violet dashed line in (b); $l = 1$]. The plot shows the absorption signatures of two elastic modes (violet symbols) and allows for the extraction of the acoustic relaxation rates $\eta_{a1/2}$ by a Lorentzian fit (red and blue lines).

## III. EXPERIMENTAL RESULTS

In Fig. 1(b), we show exemplary transmission data $|S_{21}|$ for $T = 5$, 100, and 300 K (corresponding to $l = 1$, 2, and 3) as a function of the applied magnetic field $H_{ext}$ around a center frequency of $\omega_0/(2\pi) = 18$ GHz. The parameters of the subpanels are listed in Table I. Note that the small

TABLE I. The temperature $T$ and resonance field $\mu_0 H_{res}$, as well as the minimum and maximum $S_{21}$ parameters $\min(|S_{21}^l|)$ and $\max(|S_{21}^l|)$ of the subpanels ($l = 1$, 2, and 3) presented in Fig. 1(b).

| $l$ | $T$ (K) | $\mu_0 H_{res}$ (T) | $\min(\lvert S_{21}^l\rvert)$ ($\times 10^{-3}$) | $\max(\lvert S_{21}^l\rvert)$ ($\times 10^{-3}$) |
|---|---|---|---|---|
| 1 | 5 | 3.01 | 16 | 25 |
| 2 | 100 | 3.00 | 14 | 21 |
| 3 | 300 | 2.94 | 14 | 28 |

absolute values of $|S_{21}|$ are caused by attenuation in the microwave lines. We observe the characteristic microwave response of the Kittel mode in brown color, which features a distinct pattern that is periodic along the frequency axis [visible in Fig. 1(b) for $l = 1$ and 2]. Here, we can clearly differentiate between magnetic and elastic resonance features in the $S_{21}$ data from their magnetic field dependence and frequency evolution. In detail, the magnetic response is continuous in $\omega$ and continuously varies with $H_{\mathrm{ext}}$, whereas the elastic features are only visible for discrete resonance frequencies $\omega \approx \omega_n$ and are independent of $H_{\mathrm{ext}}$. The measured transmission data clearly indicate the interaction of the homogeneous FMR mode with the equally spaced high-overtone elastic modes of the BAW resonator (cf. Refs. [32–35,52,60]). At low temperatures, we observe a double-peak signature with a periodicity of $\omega_{\mathrm{FSR}}/(2\pi) \approx 6.04$ MHz. This value agrees well with the expected frequency spacing $\omega_{\mathrm{FSR}} = 2\pi f_{\mathrm{FSR}}$ generated by standing transverse acoustic waves in the BAW resonator if we assume a total thickness $d + L$ of the resonator [61]. Here, $v_{\mathrm{t}}$ and $\tilde{v}_{\mathrm{t}}$ are the velocities of transverse elastic shear waves in the $Al_2O_3$ substrate of thickness $L$ and the CoFe film of thickness $d$, respectively. Hence, we attribute these features to the magnetization dynamics in the CoFe layer coupling individually to the two transverse acoustic modes of the sapphire layer [52]. The detection of two neighboring acoustic wave resonances with a small frequency splitting of $\Delta\omega/(2\pi) \approx 1.40$ MHz is attributed to the fact that there is a small difference of the velocities of the fast and slow transverse modes $v_{\mathrm{ft}}$ and $v_{\mathrm{st}}$ ($v_{\mathrm{ft}} - v_{\mathrm{st}} \simeq 1$ m/s) due to a small but finite angle between the $c$ axis of sapphire and the propagation direction of the shear waves, which is parallel to the surface normal [52]. For higher temperatures, e.g., $T = 100$ K ($l = 2$), the phonon resonance double features shift to lower frequencies compared to the $l = 1$ subpanel due to the thermal expansion of the sample and the temperature dependence of the elastic parameters. They also become less pronounced due to an increase in acoustic damping, which in addition results in a broadening of the acoustic wave resonances. At $T = 300$ K ($l = 3$), the interaction between magnons and the bulk acoustic resonator modes is no longer directly visible in the raw $|S_{21}|$ spectra.

To analyze these data further, we quantify the FMR line width $\Delta H$ from fixed frequency cuts in our data. Specifically, we fit $|S_{21}(H_{\mathrm{ext}})|$ to a modified form of the Polder susceptibility [22,62] represented by Eq. (A2) to extract the (half width at half maximum) line width $\Delta H$ (see Appendix B). The magnon-phonon coupling signature displayed in Fig. 1(b) presents itself as modification of the FMR line width, when displayed as fixed-frequency cuts. Figure 1(c) shows these cuts for the case when the FMR is resonant (magenta symbols) with a BAW resonator mode and when they are decoupled (blue symbols). Apparently, we observe an increase of the FMR line width when magnons and the excitations of the BAW resonator interact. Consequently, the observed resonant change in $S_{21}(H_{\mathrm{ext}})$ for phononic resonance frequencies in Fig. 1(b) is reduced compared to the off-phononic resonant case due to the enhanced magnetic damping. We quantify these FMR line-width modification by $\Delta H_{\mathrm{MEC}} = \Delta H - \Delta H_0$, referencing the observed line width to the FMR line width for the decoupled case $\Delta H_0$. Note that for quantifying magnon-phonon hybrids, the intrinsic magnon relaxation rate $\kappa_{\mathrm{s}}$ is a relevant parameter, which we determine from the FMR line width $\Delta H_0$. We find $\kappa_{\mathrm{s}}/(2\pi) = \gamma\mu_0\Delta H_0/(4\pi) = (69.0 \pm 0.1)$ MHz for $T = 5$ K and 18 GHz, which agrees well with Refs. [52,55,58,59].

The acoustic damping rates $\eta_{\mathrm{a1,a2}}$ are determined by measuring $|S_{21}(\omega)|$ at a fixed magnetic field that is off-resonant with the FMR resonance field, as indicated by the vertical dashed violet line in Fig. 1(b) ($l = 1$). The result is shown in Fig. 1(d). By detuning $H_{\mathrm{ext}}$ from the resonance field $H_{\mathrm{res}}$, we ensure that the $\eta_{\mathrm{a1,a2}}$ are not affected by the interaction with the FMR [35]. Figure 1(d) shows two absorption signatures attributed to two elastic resonances, for which we determine $\eta_{\mathrm{a1}}/(2\pi) \approx 0.23 \pm 0.01$ MHz and $\eta_{\mathrm{a2}}/(2\pi) \approx 0.16 \pm 0.01$ MHz (HWHM) by fitting the data to two Lorentzian absorption lines.

This data analysis allows us to study the loss rates of the magnetic and elastic channels of our CoFe/$Al_2O_3$ sample as a function of both the frequency and the temperature. In Figs. 2(a) and 2(b), we plot the extracted $\kappa_{\mathrm{s}}(\omega)$ and $\eta_{\mathrm{a},i}(\omega)$ values for $T = 5$K. We attribute the observed linear dependence in the magnetic relaxation rate $\kappa_{\mathrm{s}}(\omega)$ to viscous Gilbert damping. The corresponding damping parameter $\alpha$ is obtained by fitting the data presented in Fig. 1 to the expression $\kappa_{\mathrm{s}} = \kappa_{\mathrm{s0}} + 2\alpha\omega$ [63], which yields $\alpha = (2.9 \pm 0.1) \times 10^{-3}$. The inhomogeneous line width is $\kappa_{\mathrm{s0}}/(2\pi) = (48.0 \pm 2.4)$ MHz. Both values are in agreement with room-temperature values reported in Refs. [58,59] (note that in Fig. 6 we show that the magnetization damping of CoFe does not change strongly as a function of temperature).

In analogy to the room-temperature attenuation of elastic modes in GGG in Refs. [34,35], we fit the measured elastic damping of the two modes in Fig. 2(b) to

$$\eta_{\mathrm{a},i}(\omega) = \eta^0_{\mathrm{a},i} + \xi_i\omega^2. \tag{1}$$

The frequency-independent relaxation rate $\eta^0_{\mathrm{a},i}$ is assigned to mechanisms related to scattering at defects in the crystal and geometric effects, limiting the phonon confinement to the BAW resonator. The parabolic frequency dependence can be attributed to phonon-phonon scattering, as the phonon density of states scales $\propto \omega^2$ due to the linear dispersion of acoustic phonons for $\hbar\omega/k_{\mathrm{B}}T < 1$, where $\hbar$ is the reduced Planck constant and $k_{\mathrm{B}}$ is the Boltzmann constant. We obtain $\eta^0_{\mathrm{a1,a2}}/(2\pi) = (43 \pm 17)$ kHz, $(41 \pm 18)$ kHz

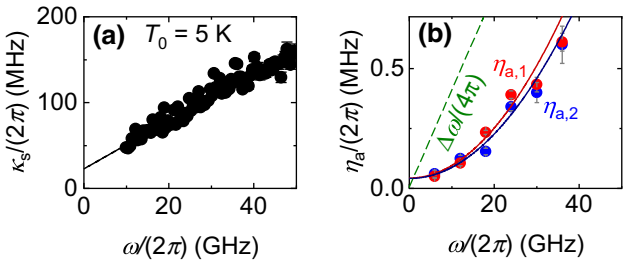


FIG. 2. The relaxation rates of the (a) magnetic and (b) elastic subsystems at $T_0 = 5$ K as a function of the frequency. The lines represent fits to the data with an (a) linear or (b) quadratic frequency dependence for the magnetic and elastic subsystems, respectively. The green dashed line corresponds to half of the frequency splitting of the two transverse elastic modes $\Delta\omega/(4\pi)$ in order to gauge the mode overlap of these two modes.

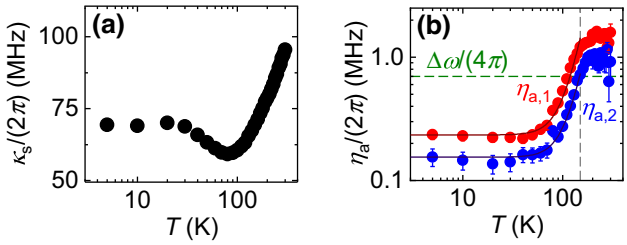


FIG. 3. The relaxation rates of the (a) magnetic and (b) elastic subsystems at $\omega/(2\pi) \approx \omega_0/(2\pi) = 18$ GHz as a function of temperature. The continuous lines in (b) represent fits to Eq. (2) and the green dashed line indicates half of the frequency splitting of the two transverse elastic modes $\Delta\omega/(4\pi)$. For $\eta_{a,i} > \Delta\omega/2$, the line width of the two transverse acoustic modes becomes larger than their frequency spacing.

and $\xi_{1/2}/(2\pi) = (1.3 \pm 0.1) \times 10^{-8}$/GHz, $(1.2 \pm 0.1) \times 10^{-8}$/GHz, which are one order of magnitude lower compared to the values found for GGG in Ref. [35] at room temperature.

The observation of pronounced standing elastic waves in BAW and Fabry-Perot resonators is expected when the effective (acoustic) decay lengths $\delta_{1/2} = v_t/\eta_{a1/2}(\omega) > 2L$. Given the frequency dependence presented in Fig. 2(b), we thus expect to meet this criterion up to $\omega/(2\pi) \simeq 50$ GHz at $T = 5$ K. The elastic relaxation rate derived from the fit in Fig. 2(b) translates into a quality factor of the BAW resonator of $Q \simeq (20\text{–}25) \times 10^3$ at $\omega/(2\pi) = 1$ GHz, which is comparable to the values of high-overtone bulk acoustic resonators reported in Refs. [64,65]. Here, we speculate that the imperfect plane parallelism of the top and bottom surface and the finite surface roughness of the substrate limit the measured $Q$ factor, as such imperfections can cause acoustic loss channels (for details, see Ref. [52]). The parabolic frequency dependence of $\eta_a$ can also be seen as an asset for the generation of helical phonons, which requires the controlled excitation of a superposition of both orthogonal shear waves by a single chiral drive (the FMR mode). For the sample investigated, we identify $\omega/2\pi < 0.8$ GHz as the frequency range in which this can be achieved [see Fig. 2(b)]. In this regime, the acoustic relaxation rate exceeds the frequency separation of the two acoustic modes, $\Delta\omega/2 < \eta_{a1,a2}$ [see the green dashed line in Fig. 2(b)]. Obviously, in this case, simultaneous excitation of the two orthogonal acoustic modes is possible. Alternatively, the temperature dependence of the elastic relaxation and the sound velocity can also be explored for this purpose, as discussed in the context of Fig. 3.

The temperature dependence of the off-resonant elastic and magnetic relaxation rates, $\kappa_s$ and $\eta_{a,i}$, in the vicinity of $\omega_0/(2\pi) = 18$ GHz is presented in Fig. 3. The magnetization-damping rate $\kappa_s$ is approximately constant up to $T = 30$ K, followed by a minimum at $T = 100$ K and a continuous increase for higher $T$. The regime $4\text{ K} < T < 100$ K matches the behavior of Permalloy in our previous studies [66,67] and theoretical predictions for the magnetic damping in $3d$ transition metals [68] and we expect the observed strong increase in $\kappa_s$ for $T > 100$ K to continue for higher temperatures. The increase of $\kappa_s$ for higher $T$ can be explained by the fact that the line width of the acoustic modes increases with $T$, resulting in a more effective phonon-pumping contribution to the magnetization relaxation [30,31] (see Appendix E). We note that the contribution of magnon-magnon scattering to $\kappa_s$ also increases with $T$, though its contribution to the FMR line width has been found to be small for $3d$ transition metals [54].

For the elastic relaxation rates $\eta_{a,i}$ in Fig. 3(b), we observe nearly constant values from 300 K down to $T \approx 180$ K. From the observed trend, we expect $\eta_{a,i}$ to remain roughly constant for temperatures above room temperature. Notably, the formation of standing acoustic waves is also detected at elevated temperatures up to room temperature at $\omega_0/(2\pi) = 18$ GHz as $\delta_{1/2}(T = \text{RT}) \approx 0.6\text{ cm}/1.0\text{ cm} \simeq 2L$. For lower temperatures, $\eta_{a1,a2}$ decrease strongly down to $T = 80$ K and remain roughly constant for lower $T$. The temperature dependence in the low-temperature regime is governed by the Landau-Rumer mechanism [50] as experimentally found in Ref. [49]. This model predicts [49]

$$\eta_{a,i}(T) = \iota^0_{a,i} + \beta_{a,i}T^4. \tag{2}$$

The comparison with our data yields the parameters $\iota^0_{a1,a2}/(2\pi) = (0.22 \pm 0.02)$ MHz, $(0.16 \pm 0.01)$ MHz and $\beta_{a1,a2}/(2\pi) = (0.97 \pm 0.03) \times 10^{-3}$ Hz/K$^4$, $(2.28 \pm 0.16) \times 10^{-3}$ Hz/K$^4$, which are in reasonable agreement with the values in Ref. [49] (see Appendix C). Note that $\iota^0_{a1,a2}$ can be limited by the imperfect plane parallelism of the substrate surfaces as well as the surface morphology [52]. For temperatures $T > 150$ K, the phonon modes are highly excited and hence we observe a roughly constant $\eta_a$ [69].

The strongly increased $\eta_a$ at elevated temperatures translates to a more pronounced mode overlap of the two transverse elastic modes, which are split in frequency by $\Delta\omega$. Under these conditions, the driving of the FMR results in a simultaneous excitation of both transverse acoustic modes and the generation of phonons with a defined circular polarization. Specifically, we identify the condition $\Delta\omega/2 \leq \eta_a$ for this process [see the green dashed line in Fig. 3(b)], which we find to be fulfilled for $T \geq 150\,\mathrm{K}$ and $\omega_0/(2\pi) = 18\,\mathrm{GHz}$. This underlines the potential of engineering the relative orientation of the plane-parallel substrate surfaces with respect to the crystallographic directions in order to achieve an efficient generation of phonons with circular polarization.

Next, we focus on the quantification of the coupling rate between the FMR mode and the resonant modes of the BAW resonator. To this end, we model the coupled system following the approach in Refs. [32,34,52] [see Eq. (D1) and Appendix D]. Solving for the amplitude of the magnetic excitation $m_{x,y}$ allows us to express the recorded FMR absorption line as a Lorentzian with a probe-frequency-dependent line width $\Delta H_{\mathrm{MEC}}$ corresponding to the loss rate [70] [see also Fig. 1(c)]

$$\tilde{\kappa}_s(\omega) = \kappa_s(\omega) + \frac{\eta_{a,i} g_{\mathrm{eff}}^2}{4[(\omega-\omega_n)^2 + \eta_{a,i}^2].} \tag{3}$$

Here, we convert from magnetic field to frequency using $\omega = (g\mu_B/\hbar)\mu_0 H_{\mathrm{ext}}$, using $g = 2.079$. Equation (3) in combination with the extracted elastic relaxation rates $\eta_{a,i}$ and the undisturbed FMR line width $\kappa_s(\omega)$ allows us to extract the effective coupling rate $g_{\mathrm{eff}}$ from the frequency evolution of the FMR line width $\Delta H_{\mathrm{MEC}}$.

Figures 4(a) and 4(b) (see also Appendix D) shows $g_{\mathrm{eff}}$ as a function of $\omega$ at $T_0 = 5$ K and as a function of $T$ for $\omega_0/(2\pi) = 18$ GHz. We observe an increase in $g_{\mathrm{eff}}$ with increasing $\omega$. This behavior is corroborated by the theoretical model presented in Refs. [30,32,35], which describes the mode overlap between the magnetic and the mechanical mode. In detail,

$$g_{\mathrm{eff}}(\omega) = B\sqrt{\frac{2g\mu_B}{\hbar\omega M_s \tilde{\rho} d L}}\left[1 - \cos\left(\omega\frac{d}{\tilde{v}_t}\right)\right], \tag{4}$$

where $M_s$ is the saturation magnetization and $\tilde{\rho}$ is the volume density of the CoFe layer. For a quantitative comparison, we use the following material and design parameters: $M_s = M_{\mathrm{eff}} = 1.90 \times 10^6$ A/m, $g = 2.079$ [71] and $d = 30\,\mathrm{nm}$, as well as the transverse velocity $\tilde{v}_t = 3170\,\mathrm{m/s}$ [52] and the volume density $\tilde{\rho} = 8110\,\mathrm{kg/m^3}$ of the CoFe layer at room temperature [72]. In addition, we use $L = 510\,\mu\mathrm{m}$. Fitting Eq. (4) to the data presented in Fig. 4(a) yields the magnetoelastic coupling constant $B = (13.5 \pm 0.6) \times 10^6$ J/m$^3$, $(12.3 \pm 0.8) \times 10^6$ J/m$^3$, which

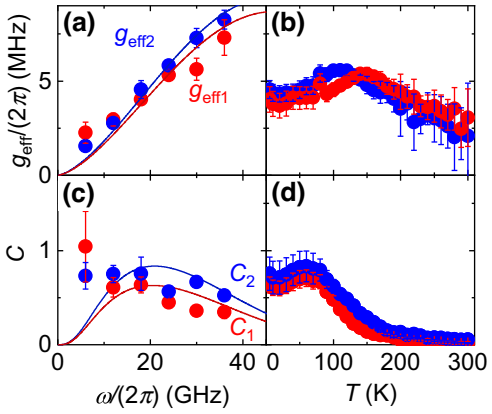


FIG. 4. (a),(b) The magnetoelastic coupling rate $g_{\mathrm{eff}}$ as a function of (a) $\omega$ and (b) temperature $T$. (c),(d) The sample cooperativity $C$ at $\omega_0/(2\pi) = 18$ GHz as a function of (c) $\omega$ and (d) $T$. $T_0 = 5$ K. The continuous lines in (a) and (b) represent fitting curves to Eqs. (4) and $C = g_{\mathrm{eff}}^2/(2\eta_{a,i}\kappa_s)$ using the fitting results of Fig. 2.

is consistent for the two transversal phonon branches and slightly lower than $B = 15.7 \times 10^6$ J/m$^3$, which we have estimated for the alloy composition [52]. As we record a maximum $\eta_{a,i}/(2\pi) < 1\mathrm{MHz} < g_{\mathrm{eff}}/(2\pi)$, we are operating in a regime corresponding to the Purcell-enhanced regime in the experimentally investigated frequency range ($5\,\mathrm{GHz} \leq f \leq 50\,\mathrm{GHz}$) at $T = 5$ K [73]. Notably, as the magnetoelastic coupling rates of the out-of-plane and in-plane geometry are related via the magnetic ellipticity of the CoFe layer [30], we expect the same temperature and frequency dependence for $g_{\mathrm{eff}}$ for the in-plane geometry—with, however, lower effective coupling rates. In Fig. 4(c), we plot the cooperativity $C_{1/2} = g_{\mathrm{eff}}^2/(2\kappa_s\eta_{a1,a2})$ as a function of $\omega$. Here, the continuous lines represent the calculated $C$ using our fitted $\eta_{a,i}$ described by Eq. (1), $g_{\mathrm{eff}}$ from Eq. (4) and using the parametrized magnetic linewidth evolution $\kappa_s(\omega)$ obtained from Fig. 2(a). Note that the maximum cooperativity is obtained around 18 GHz and does not coincide with a maximum in $g_{\mathrm{eff}}$ from Eq. (4) due to the frequency dependence of $\eta_{a,i}$ (see also Ref. [32]). We observe good agreement between theory and experiment for $\omega/(2\pi) > 15$ GHz but we do not observe the predicted reduction in $C$ for lower frequencies. We note that the discrepancy between theory and experiment appears particularly large for the cooperativity $C$ in Fig. 4(c) as it scales quadratically with $g_{\mathrm{eff}}$. As is evident in Fig. 4(a), we can attribute this to the larger values of $g_{\mathrm{eff}}$ at low $\omega$ extracted from the experiment as compared to the theoretical expected values.

In Fig. 4(b), we plot the temperature dependence of $g_{\mathrm{eff}}$ at 18GHz. Simplistically, we would expect a temperature-independent behavior, as $g_{\mathrm{eff}}$ originates from the mode overlap. However, we observe a slight increase with increasing $T$, which results in a maximum in $g_{\mathrm{eff}}$ at 150 K

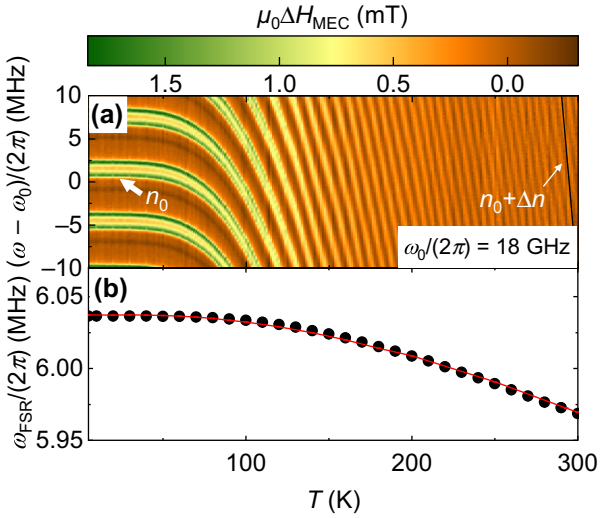


FIG. 5. (a) The fitted change in the FMR line width $\Delta H$ as a function of $T$ around $\omega_0/(2\pi) = 18$ GHz. (b) The free spectral range $\omega_{FSR}$ as a function of $T$. The red continuous line represents a theory curve for the temperature dependence of $\omega_{FSR}(T)$ using Eq. (5).

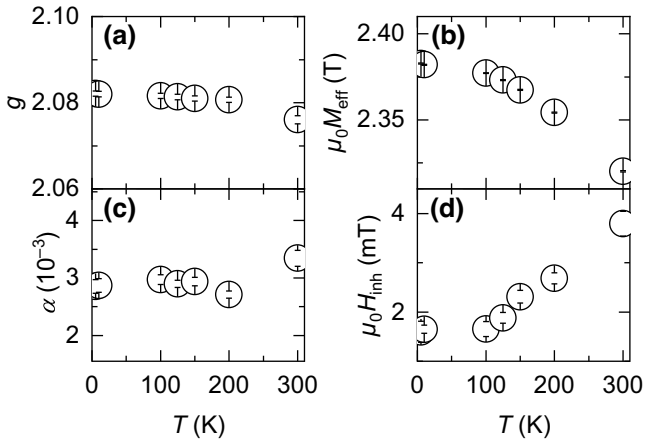


FIG. 6. Temperature dependence of the parameters in the CoFe thin film deposited on an $Al_2O_3$ substrate. (a) As expected, the $g$ factor is approximately independent of $T$. (b) The effective magnetization $M_{eff}$ decreases with increasing temperature due to the thermal excitation of magnons. (c) The Gilbert damping $\alpha$ is approximately constant as a function of the temperature. (d) The inhomogeneous line-width broadening $H_{inh}$ as a function of $T$. We observe a slight increase in $H_{inh}$ with increasing $T$, which we attribute to nonlinear damping induced by thermal magnons.

for mode 1 and at 110 K for mode 2. We attribute this to variations of the acoustic properties of the CoFe thin film and sapphire substrate, which at the peak position results in a minimum mismatch of their acoustic impedances ($Z = \sqrt{\rho v_t}$) and thereby allows for the more efficient injection of phonons for $Z_{CoFe} = Z_{Al_2O_3}$ [31]. The reduction in $g_{eff}(T)$ for higher temperatures is in agreement with the expected reduction of $B$ for $3d$ transition metals at elevated $T$ [51]. Consequently, we expect $g_{eff}(T)$ to decrease with rising temperatures as we go above room temperature. The potential presence of minima in $g_{eff}$ and $C$ in Figs. 4(b) and 4(d) at $T \simeq 10$ K are interpreted as fluctuations in the measurement data. Within the experimental error, the values for $g_{eff}$ and cooperativity $C$ are about constant in the low-temperature range ($T \leq 50$ K).

Comparing the evolution of $g_{eff}(T)$ with $\eta_a(T)$ in Fig. 3(b), we find $g_{eff} > \eta_a$ for $T < 130$ K for mode 1 and $T < 160$ K for mode 2. For the temperature dependence of the cooperativity in Fig. 4(d), we observe a peak at around 60 K, which can be tracked to the reduced $\kappa_s$ in this temperature range [see Fig. 3(a)], followed by a strong decrease with increasing temperatures, mirroring the increase in the $\eta_{a,i}$ in this temperature range [see Fig. 3(b)].

To map out the temperature evolution of the BAW resonances, we plot the FMR line-width change $\Delta H_{MEC} = \Delta H - \Delta H_0$ in Fig. 5. Here, $\Delta H_0$ is the uncoupled FMR line width around $\omega_0/(2\pi) = 18$ GHz, which is a function of the temperature and the frequency, and $\Delta H$ is the FMR line width obtained via Eq. (A2). At resonant coupling (see Fig. 1), the line width $\Delta H$ increases by $\Delta H_{MEC}$ due to the coupling of the FMR mode to the acoustic mode, appearing as an additional dissipation channel. The representation used in Fig. 5 also allows us to visualize resonant magnon-phonon coupling up to room temperature. We observe that the peaks in $\Delta H_{MEC}$ broaden for increasing $T$ and merge for temperatures $T > 120$ K. In addition, we observe that the peaks shift to lower frequencies above 75 K. As we do not selectively track one bulk acoustic resonance, we also find higher-mode bulk acoustic resonance harmonics within the spectrum. In detail, for the displayed frequency window, we count the transit of $\Delta n = 35$ bulk acoustic modes when varying the temperature between $T = 5$ K and $T = 295$ K.

In addition to the two prominent MEC features with positive $\Delta H_{MEC}$, we also find a faint signature with $\Delta H_{MEC} < 0$ for $T < 100$ K. We attribute this feature to the coupling of the Kittel mode to standing waves in the substrate of an unexpected additional phononic branch with a slightly altered propagation velocity compared to the two transverse elastic modes. Seemingly, the reduction of the bare FMR line width suggests that the elastic mode reduces the FMR damping, potentially due to a mode-interference effect. From the evolution of the MEC features of $\Delta H_{MEC}$ in Fig. 5(a), we can extract the free spectral range $\omega_{FSR}(T)$ as shown in Fig. 5(b) and compare its temperature dependence with the expected behavior of $\omega_{FSR}(T)$ modeled by

$$\omega_{n,i} = n\pi/[(d/\tilde{v}_t + L(T)/v_t(T))]. \quad (5)$$

As the thickness of the FM layer ($d \approx 30$ nm) is thin compared to that of the substrate ($L \approx 510\,\mu$m), we expect that the temperature dependence of the acoustic properties will be dominated by the substrate properties. In detail,

the transverse velocity is given by $v_t(T) = \sqrt{G(T)/\rho(T)}$, where $G(T)$ and $\rho(T)$ are the shear modulus and the volume density of the substrate. By accounting for the temperature dependence in $\rho(T)$ and $L(T)$ via the thermal-expansion coefficient $\alpha^*(T)$ using Ref. [74, Eq. (6)] and the temperature evolution of $G(T)$ [75], we can calculate the expected behavior for $\omega_{FSR}(T)$ [solid line in Fig. 5(b)]. The result corroborates the experimental observations. Notably, by monitoring the temperature dependence of the high-overtone BAW resonances, we are able to observe changes in $\omega_{FSR}/(2\pi)$ down to the kilohertz frequency range, which, according to Eq. (5) in combination with the parameters $L \simeq 510$ μm and $v_t \simeq 6.1$ km/s, translates to a relative change in substrate thickness of $\Delta L/L \approx 1.7 \times 10^{-4}$. This value is comparable to the sensitivity of high-precision strain sensors [76,77].

## IV. CONCLUSIONS AND OUTLOOK

In summary, we have studied the magnetoelastic coupling phenomena in CoFe/crystalline sapphire hybrid samples. In particular, we have extracted the frequency and temperature dependence of both the magnetic and elastic loss rates $\kappa_s$ and $\eta_a$ as well as the effective magnetoelastic coupling rate $g_{eff}$ and the cooperativity $C$ from broadband magnetic resonance experiments. We have also identified optimal working points for the realization of magnetoelastic devices. Here, in particular, the strong increase in the elastic loss rates $\eta_a$ with increasing $T$ demonstrates the advantage of performing these experiments at cryogenic temperatures to push coupled magnon-phonon systems to stronger coupling regimes, such as the high-cooperativity Purcell-enhanced regime [73]. From a different perspective, the strong increase of $\eta_a$ at elevated temperatures gives rise to a substantial mode overlap of the two transverse elastic waves, which is a prerequisite for the generation of circularly polarized phonons in the nonmagnetic crystal. Hence, in particular, the sample temperature can be viewed as a control knob for the controlled pumping of either circular or linear phonons. Regarding the magnetic loss rate, we find an almost temperature-independent Gilbert damping, which renders the CoFe/$Al_2O_3$ material platform superior to the conventionally used YIG/GGG system [32–35] regarding their performance at cryogenic temperatures. Finally, the evolution of the free spectral range has $\omega_{FSR}$ allowed us to study the temperature dependence of the thermal expansion coefficient and shear modulus with high sensitivity. This allows us to use CoFe/BAW resonators for the realization of magnetic microactuators and systems (MAGMAS) [78–81].

## ACKNOWLEDGMENTS

We acknowledge financial support by the Deutsche Forschungsgemeinschaft (DFG, German Research Foundation) via Germany's Excellence Strategy EXC-2111-390814868 and the Transregio "Constrained Quantum Matter" (TRR 360, Project-ID 492547816). This research is part of the Munich Quantum Valley, which is supported by the Bavarian State Government with funds from the Hightech Agenda Bayern Plus.

## APPENDIX A: ANALYSIS OF THE FERROMAGNETIC RESONANCE LINE SHAPE

The Polder susceptibility of the ferromagnetic resonance for a static magnetic field applied along the surface normal of a magnetic thin film, i.e., the out-of-plane (oop) geometry, is given by [31,62,66]

$$\hat{\chi}_P = \begin{pmatrix} \chi_{xx} & \chi_{xy} \\ \chi_{yx} & \chi_{yy} \end{pmatrix} = \frac{\mu_0 M_s}{\Delta(\omega)} \times \begin{pmatrix} \gamma\mu_0(H_{ext} - M_s) - i\kappa_s & -i\omega \\ i\omega & \gamma\mu_0(H_{ext} - M_s) - i\kappa_s \end{pmatrix}, \tag{A1}$$

assuming a negligible uniaxial anisotropy constant $K_u = 0$. Here, $\Delta(\omega)$ is the determinant of $\hat{\chi}_P$, $M_s$ is the saturation magnetization, $H_{ext}$ is the externally applied static magnetic field, $\kappa_s$ is the FMR line width, and $\mu_0$ is the magnetic vacuum permeability. We fit our experimental spectroscopy data $S_{21}(H_{ext})|_\omega$ shown in exemplary form in Fig. 1(c) using

$$S_{21}(H_{ext})|_\omega = C_0 + C_1 H_{ext} - iAe^{i\phi}\frac{\chi_{yy}(H_{ext})}{\mu_0 M_s}. \tag{A2}$$

To account for the complex microwave transmission background $S_{21}^0$ in our experiments, we include a linear function of the form $S_{21}^0 = C_0 + C_1 H_{ext}$ with the complex offset $C_0$ and slope $C_1$, following the approach used in Refs. [63,66]. Furthermore, in Eq. (A2), $A$ is an amplitude and $\phi$ is a phase factor describing the microwave detection circuit.

## APPENDIX B: TEMPERATURE DEPENDENCE OF THE MAGNETIC RESONANCE PARAMETERS OF CoFe

Figure 6 summarizes the temperature dependence of parameters describing the magnetization dynamics of the CoFe thin film, which is deposited on a $Al_2O_3$ substrate and investigated in the main text. The $g$ factor displayed in Fig. 6(a) shows only a minimal decrease with increasing $T$. The effective magnetization $M_{eff}$ presented in Fig. 6(b) decreases for increasing temperature due to the thermal excitation of magnons. To assess the magnetization damping properties, we analyze the frequency dependence of the FMR line width using [63]

$$\kappa_s = \kappa_{s0} + 2\alpha\omega. \tag{B1}$$

Here, $\kappa_{s0}$ represents the inhomogeneous line width and $\alpha$ is the Gilbert damping parameter. We note that the Gilbert

damping parameter $\alpha$ [see Fig. 6(c)] is approximately temperature independent, while we observe a slight increase in the inhomogeneous line width $H_{\mathrm{inh}} = (\hbar\kappa_{\mathrm{s0}}/g\mu_0\mu_B)$ for increasing temperatures [see Fig. 6(d)], which we attribute to nonlinear damping induced by thermal magnons.

## APPENDIX C: TEMPERATURE DEPENDENCE OF THE ELASTIC DAMPING

For the Landau-Rumer mechanism, the attenuation coefficient $\nu(T)$ of the transverse elastic waves is given by [49]

$$\nu(T) = 60\gamma_{\mathrm{G}}^2 \frac{k_{\mathrm{B}}}{M v_{\mathrm{t}}^3 \Theta_{\mathrm{D}}^3} \omega T^4, \tag{C1}$$

where $\Theta_{\mathrm{D}}$ is the Debye temperature, $\gamma_{\mathrm{G}}$ is the Grüneisen parameter, and $M$ is the average atomic mass. Using the attenuation coefficient $\nu(T)$ in combination with the characteristic decay length $\delta_{\mathrm{LR}} = v_{\mathrm{t}}/\eta_{\mathrm{a}}$ [32], defined as the distance at which the amplitude of the phonon mode has decayed to $1/e$ of its initial value, we can determine the elastic relaxation rate by using

$$\frac{|u(\delta_{\mathrm{LR}})|}{|u(0)|} = \exp(-\nu\delta_{\mathrm{LR}}) = \exp(-1). \tag{C2}$$

Here, $|u(z')|$ is the magnitude of the acoustic modes after propagating a distance $z'$ through the $Al_2O_3$ substrate in the $z$ direction. From Eq. (C2), we obtain the relation $\eta_{\mathrm{a}} = \nu v_{\mathrm{t}} = \beta_{\mathrm{a}} T^4$. By inserting $\gamma_{\mathrm{G}} = 2$, $(M v_{\mathrm{t}}^2/k_{\mathrm{B}}) = 135\,000$ K, and $\Theta_{\mathrm{D}} = 1000$ K from Ref. [49] and $v_{\mathrm{t}} = 6.17$ km/s [52] in Eq. (C1), we obtain $\beta_{\mathrm{a}}/(2\pi) \approx 3.2 \times 10^{-2}$ Hz/K$^4$, which is in reasonable agreement with the obtained fitting values $\beta_{\mathrm{a1,a2}}/(2\pi) = (0.97 \pm 0.03) \times 10^{-3}$ Hz/K$^4$, $(2.28 \pm 0.16) \times 10^{-3}$ Hz/K$^4$ in the main text.

## APPENDIX D: DETERMINATION OF THE EFFECTIVE COUPLING RATE FROM THE FREQUENCY DEPENDENT FMR LINE WIDTH

When the FMR mode couples resonantly to an acoustic mode of the BAW resonator, the resulting line-width modification $\Delta H_{\mathrm{MEC}}$ allows us to quantify the magnon-phonon coupling strength $g_{\mathrm{eff}}$. Here, we derive an explicit expression for the FMR line-width evolution as a function of the probe frequency $\omega$. To this end, we use the same formalism as in Ref. [32] and describe our FM–BAW resonator system as interacting harmonic resonators. In particular, we only consider one individual elastic BAW-mode coupling to the magnetic Kittel mode. The differential equations describing this model read as follows:

$$\begin{aligned}(\omega - \omega_{\mathrm{mag}} + i\kappa_{\mathrm{s}})m^{\mathrm{x,y}} &= g_{\mathrm{eff}} u_n^{\mathrm{x,y}}/2 + \zeta h^{\mathrm{x,y}} \\ (\omega - \omega_n + i\eta_{\mathrm{a}})u_n^{\mathrm{x,y}} &= g_{\mathrm{eff}} m^{\mathrm{x,y}}/2.\end{aligned} \tag{D1}$$

Here, $\omega$ is the microwave probe frequency, $\omega_{\mathrm{mag}}$ is the magnetic resonance frequency, $\omega_n$ is the resonance frequency of the elastic mode, $\eta_{\mathrm{a}}$ ($\kappa_{\mathrm{s}}$) is the damping rate of the elastic (magnetic) system, and $u^{\mathrm{x,y}}$ ($m^{\mathrm{x,y}}$) are the amplitudes of the elastic (magnetic) excitations. Note that $\omega_n$ is connected to the phonon-propagation velocities via Eq. (5). The parameter $\zeta$ describes the inductive coupling to the antenna and $h^{\mathrm{x}}$ and $h^{\mathrm{y}}$ are the in- and out-of-phase amplitudes of the microwave magnetic field generated by the coplanar waveguide. We solve Eq. (D1) for $m^{\mathrm{x,y}}$ and obtain

$$m^{\mathrm{x,y}} = -\zeta h^{\mathrm{x,y}} \frac{(\omega - \omega_n + i\eta_{\mathrm{a}})}{(\omega - \omega_n + i\eta_{\mathrm{a}})(\omega - \omega_{\mathrm{mag}} + i\kappa_{\mathrm{s}}) + g_{\mathrm{eff}}^2/4}. \tag{D2}$$

We can rewrite this expression as

$$m^{\mathrm{x,y}} = -\frac{\zeta h^{\mathrm{x,y}}}{(\omega - \omega_{\mathrm{mag}}) - g_{\mathrm{eff}}^2/(4C(\omega))(\omega - \omega_n) + i[\kappa_{\mathrm{s}} + g_{\mathrm{eff}}^2\eta_{\mathrm{a}}/(4C(\omega))]}, \tag{D3}$$

where we have defined $C(\omega) = (\omega - \omega_n)^2 + \eta_{\mathrm{a}}^2$. The imaginary part in the denominator of Eq. (D3) can be interpreted as a modified magnetic relaxation rate $\tilde{\kappa}_{\mathrm{s}}$ in the presence of magnetoelastic coupling and is given by

$$\tilde{\kappa}_{\mathrm{s}} = \kappa_{\mathrm{s}} + \frac{\eta_{\mathrm{a}} g_{\mathrm{eff}}^2}{4[(\omega - \omega_n)^2 + \eta_{\mathrm{a}}^2]}. \tag{D4}$$

In resonance with the phononic modes, we obtain

$$\tilde{\kappa}_{\mathrm{s}}(\omega = \omega_n) = \kappa_{\mathrm{s}} + \frac{g_{\mathrm{eff}}^2}{4\eta_{\mathrm{a}}}. \tag{D5}$$

Alternatively,

$$\begin{aligned} g_{\mathrm{eff}} &= 2\sqrt{\eta_{\mathrm{a}}(\tilde{\kappa}_{\mathrm{s}}(\omega = \omega_n) - \kappa_{\mathrm{s}})} \\ &= \sqrt{2\eta_{\mathrm{a}}\gamma[\mu_0(\Delta H(\omega = \omega_n) - \Delta H_0)]}. \end{aligned} \tag{D6}$$

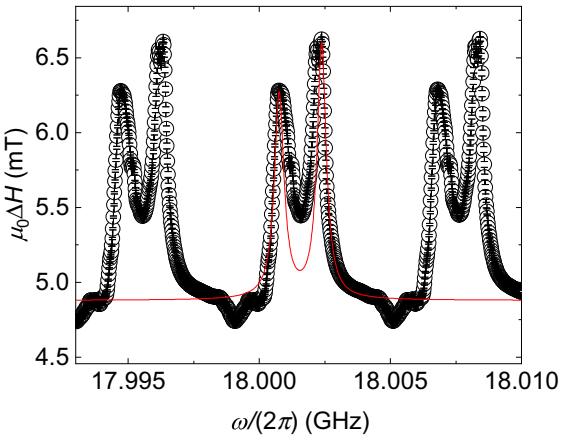


FIG. 7. FMR line width $\Delta H$ of a CoFe thin film deposited on a $Al_2O_3$ substrate plotted as a function of $\omega$ around $\omega_0/(2\pi) = 18$ GHz at $T = 5$ K. The continuous red line indicates a plot of the line-width modulation following Eq. (3) and using the extracted values for $\kappa_s$, $\eta_{a1,a2}$ and $g_{eff1/2}$, using the sum of the two individual resonances with $\omega_{n1}/(2\pi) = 18.0008$ GHz and $\omega_{n2}/(2\pi) = 18.0024$ GHz.

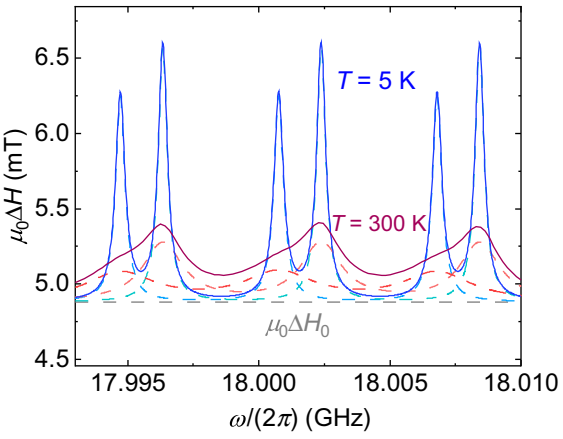


FIG. 8. Theory curve for the FMR line width using Eq. (E1) as a function of $\omega$ around $\omega/(2\pi) = 18$ GHz for cryogenic temperatures (blue line) and room temperature (red line). Periodic double-peak features are observed. The dotted blue and red lines indicate the individual contributions of $\tilde{\kappa}_{s1}$ and $\tilde{\kappa}_{s2}$ at 5 K and 300 K.

Hence, in our experiments, the effective coupling rate between the Kittel mode and the elastic modes of the acoustic resonator can be determined from the resonant change of the FMR line width.

In Fig. 7, we plot the line-width modulation of the FMR line width $\Delta H$ as a function of the microwave frequency around 18 GHz at $T = 5$ K. The continuous red line represents the calculated line-width modulation following Eq. (3) together with the extracted values for $\kappa_s$, $\eta_{a1,a2}$, and $g_{eff1/2}$ from the main text and plotting the sum of the two individual resonances with resonance frequencies at $\omega_{n1}/(2\pi) = 18.0008$ GHz and $\omega_{n2}/(2\pi) = 18.0024$ GHz for the two transverse elastic modes. We observe good quantitative agreement between Eq. (3) and our experimental data. Discrepancies are apparent, in particular, in the frequency range between the two resonances, which indicates that a more sophisticated model, which accounts for the interaction of the two transverse modes, is required to properly describe the modulation of $\Delta H(\omega)$ in this frequency range.

## APPENDIX E: PHONON-PUMPING CONTRIBUTION TO THE FMR LINE WIDTH

Using Eq. (3), we study the temperature dependence of the impact of magnetoelastic coupling on the FMR line width $\Delta H$. As we couple to two phonon modes in our experiment, we define the net $\tilde{\kappa}_s(\omega)$ in our experiment as

$$\tilde{\kappa}_s(\omega) = \tilde{\kappa}_{s1}(\omega, \eta_{a/1}, v_{ft}) + \tilde{\kappa}_{s2}(\omega, \eta_{a/2}, v_{st}). \tag{E1}$$

The resulting impact on the FMR line width $\Delta H$ for $T = 5$ K and $T = 300$ K, when using the extracted $\eta_{a,i}(\omega)$ for the respective temperature from Fig. 3(b), is plotted in Fig. 8.

In Fig. 8, we observe periodic double-peak features induced from the coupling of the FMR with the two elastic resonances, which are particularly pronounced for the $T = 5$ K case due to the small line width of the elastic resonances. For $T = 300$ K, the resonance peaks broaden and overlap. Notably, due to their strongly increased elastic damping, $\tilde{\kappa}_s$ takes nonzero values even for off-resonant $\omega$ values. Consequently, the net FMR line width $\Delta H$ increases for elevated temperatures.

[1] E. G. Spencer and R. C. LeCraw, Magnetoacoustic resonance in yttrium iron garnet, Phys. Rev. Lett. **1**, 241 (1958).
[2] A. Widom, C. Vittoria, and S. D. Yoon, Gilbert ferromagnetic damping theory and the fluctuation-dissipation theorem, J. Appl. Phys. **108**, 073924 (2010).
[3] C. Vittoria, S. D. Yoon, and A. Widom, Relaxation mechanism for ordered magnetic materials, Phys. Rev. B **81**, 014412 (2010).
[4] E. Rossi, O. G. Heinonen, and A. H. MacDonald, Dynamics of magnetization coupled to a thermal bath of elastic modes, Phys. Rev. B **72**, 174412 (2005).
[5] T. Kobayashi, R. C. Barker, and A. Yelon, Ferromagnetoelastic resonance in thin films. II. Application to nickel, Phys. Rev. B **7**, 3286 (1973).
[6] T. Kobayashi, R. C. Barker, J. L. Bleustein, and A. Yelon, Ferromagnetoelastic resonance in thin films. I. Formal treatment, Phys. Rev. B **7**, 3273 (1973).
[7] S. Klingler, H. Maier-Flaig, C. Dubs, O. Surzhenko, R. Gross, H. Huebl, S. T. B. Goennenwein, and M. Weiler, Gilbert damping of magnetostatic modes in a yttrium iron garnet sphere, Appl. Phys. Lett. **110**, 092409 (2017).

[8] M. Weiler, L. Dreher, C. Heeg, H. Huebl, R. Gross, M. S. Brandt, and S. T. B. Goennenwein, Elastically driven ferromagnetic resonance in nickel thin films, Phys. Rev. Lett. **106**, 117601 (2011).

[9] M. Weiler, H. Huebl, F. S. Goerg, F. D. Czeschka, R. Gross, and S. T. B. Goennenwein, Spin pumping with coherent elastic waves, Phys. Rev. Lett. **108**, 176601 (2012).

[10] P. G. Gowtham, G. M. Stiehl, D. C. Ralph, and R. A. Buhrman, Thickness-dependent magnetoelasticity and its effects on perpendicular magnetic anisotropy in Ta/CoFeB/MgO thin films, Phys. Rev. B **93**, 024404 (2016).

[11] M. Küß, M. Heigl, L. Flacke, A. Hörner, M. Weiler, M. Albrecht, and A. Wixforth, Nonreciprocal Dzyaloshinskii-Moriya magnetoacoustic waves, Phys. Rev. Lett. **125**, 217203 (2020).

[12] M. Küß, M. Heigl, L. Flacke, A. Hefele, A. Hörner, M. Weiler, M. Albrecht, and A. Wixforth, Symmetry of the magnetoelastic interaction of Rayleigh and shear horizontal magnetoacoustic waves in nickel thin films on LiTa O3, Phys. Rev. Appl. **15**, 1 (2021).

[13] M. Küß, M. Heigl, L. Flacke, A. Hörner, M. Weiler, A. Wixforth, and M. Albrecht, Nonreciprocal magnetoacoustic waves in dipolar-coupled ferromagnetic bilayers, Phys. Rev. Appl. **15**, 1 (2021).

[14] T. Kikkawa, K. Shen, B. Flebus, R. A. Duine, K.-I. Uchida, Z. Qiu, G. E. Bauer, and E. Saitoh, Magnon polarons in the spin Seebeck effect, Phys. Rev. Lett. **117**, 207203 (2016).

[15] Y. Hashimoto, T. H. Johansen, and E. Saitoh, 180°-phase shift of magnetoelastic waves observed by phase-resolved spin-wave tomography, Appl. Phys. Lett. **112**, 232403 (2018).

[16] X. Zhang, A. Galda, X. Han, D. Jin, and V. M. Vinokur, Broadband nonreciprocity enabled by strong coupling of magnons and microwave photons, Phys. Rev. Appl. **13**, 044039 (2020).

[17] D. Hatanaka, M. Asano, H. Okamoto, Y. Kunihashi, H. Sanada, and H. Yamaguchi, On-chip coherent transduction between magnons and acoustic phonons in cavity magnomechanics, Phys. Rev. Appl. **17**, 034024 (2022).

[18] M. Weiler, A. Brandlmaier, S. Geprägs, M. Althammer, M. Opel, C. Bihler, H. Huebl, M. S. Brandt, R. Gross, and S. T. B. Goennenwein, Voltage controlled inversion of magnetic anisotropy in a ferromagnetic thin film at room temperature, New J. Phys. **11**, 013021 (2009).

[19] K. Uchida, H. Adachi, T. An, T. Ota, M. Toda, B. Hillebrands, S. Maekawa, and E. Saitoh, Long-range spin Seebeck effect and acoustic spin pumping, Nat. Mater. **10**, 737 (2011).

[20] L. Thevenard, C. Gourdon, J. Y. Prieur, H. J. von Bardeleben, S. Vincent, L. Becerra, L. Largeau, and J.-Y. Duquesne, Surface-acoustic-wave-driven ferromagnetic resonance in (Ga, Mn) (As, P) epilayers, Phys. Rev. B **90**, 094401 (2014).

[21] L. Thevenard, J.-Y. Duquesne, E. Peronne, H. J. von Bardeleben, H. Jaffres, S. Ruttala, J.-M. George, A. Lemaître, and C. Gourdon, Irreversible magnetization switching using surface acoustic waves, Phys. Rev. B **87**, 144402 (2013).

[22] L. Dreher, M. Weiler, M. Pernpeintner, H. Huebl, R. Gross, M. S. Brandt, and S. T. B. Goennenwein, Surface acoustic wave driven ferromagnetic resonance in nickel thin films: Theory and experiment, Phys. Rev. B **86**, 134415 (2012).

[23] Q. ul ain, D. Odkhuu, S. H. Rhim, and S. C. Hong, Enhanced voltage-controlled magnetic anisotropy via magnetoelasticity in FePt/MgO(001), Phys. Rev. B **101**, 214436 (2020).

[24] L. Bi, H.-S. Kim, G. F. Dionne, and C. A. Ross, Structure, magnetic properties and magnetoelastic anisotropy in epitaxial $Sr(Ti_{1-x}Co_x)O_3$ films, New J. Phys. **12**, 043044 (2010).

[25] K. An, X. Ma, C.-F. Pai, J. Yang, K. S. Olsson, J. L. Erskine, D. C. Ralph, R. A. Buhrman, and X. Li, Current control of magnetic anisotropy via stress in a ferromagnetic metal waveguide, Phys. Rev. B **93**, 140404 (2016).

[26] R. Yahiro, T. Kikkawa, R. Ramos, K. Oyanagi, T. Hioki, S. Daimon, and E. Saitoh, Magnon polarons in the spin Peltier effect, Phys. Rev. B **101**, 024407 (2020).

[27] A. S. Sukhanov, M. S. Pavlovskii, P. Bourges, H. C. Walker, K. Manna, C. Felser, and D. S. Inosov, Magnon-polaron excitations in the noncollinear antiferromagnet $Mn_3Ge$, Phys. Rev. B **99**, 214445 (2019).

[28] H. Hayashi and K. Ando, Spin pumping driven by magnon polarons, Phys. Rev. Lett. **121**, 237202 (2018).

[29] A. Brataas, B. van Wees, O. Klein, G. de Loubens, and M. Viret, Spin insulatronics, Phys. Rep. **885**, 1 (2020).

[30] S. Streib, H. Keshtgar, and G. E. Bauer, Damping of magnetization dynamics by phonon pumping, Phys. Rev. Lett. **121**, 027202 (2018).

[31] T. Sato, W. Yu, S. Streib, and G. E. W. Bauer, Dynamic magnetoelastic boundary conditions and the pumping of phonons, Phys. Rev. B **104**, 014403 (2021).

[32] K. An, A. N. Litvinenko, R. Kohno, A. A. Fuad, V. V. Naletov, L. Vila, U. Ebels, G. De Loubens, H. Hurdequint, N. Beaulieu, J. Ben Youssef, N. Vukadinovic, G. E. Bauer, A. N. Slavin, V. S. Tiberkevich, and O. Klein, Coherent long-range transfer of angular momentum between magnon Kittel modes by phonons, Phys. Rev. B **101**, 1 (2020).

[33] K. An, R. Kohno, A. N. Litvinenko, R. L. Seeger, V. V. Naletov, L. Vila, G. de Loubens, J. Ben Youssef, N. Vukadinovic, G. E. W. Bauer, A. N. Slavin, V. S. Tiberkevich, and O. Klein, Bright and dark states of two distant macrospins strongly coupled by phonons, Phys. Rev. X **12**, 011060 (2022).

[34] K. An, C. Kim, K.-W. Moon, R. Kohno, G. Olivetti, G. de Loubens, N. Vukadinovic, J. Ben Youssef, C. Hwang, and O. Klein, Optimizing the magnon-phonon cooperativity in planar geometries, Phys. Rev. Appl. **20**, 014046 (2023).

[35] R. Schlitz, L. Siegl, T. Sato, W. Yu, G. E. W. Bauer, H. Huebl, and S. T. B. Goennenwein, Magnetization dynamics affected by phonon pumping, Phys. Rev. B **106**, 014407 (2022).

[36] S. Sharma, V. S. V. Bittencourt, and S. Viola Kusminskiy, Protocol for generating an arbitrary quantum state of the magnetization in cavity magnonics, J. Phys. Mater. **5**, 034006 (2022).

[37] V. A. S. V. Bittencourt, I. Liberal, and S. Viola Kusminskiy, Optomagnonics in dispersive media: Magnon-photon coupling enhancement at the epsilon-near-zero frequency, Phys. Rev. Lett. **128**, 183603 (2022).

[38] V. Wachter, V. A. S. V. Bittencourt, S. Xie, S. Sharma, N. Joly, P. S. Russell, F. Marquardt, and S. V. Kusminskiy,

Optical signatures of the coupled spin-mechanics of a levitated magnetic microparticle, J. Opt. Soc. Am. B **38**, 3858 (2021).

[39] C. A. Potts, E. Varga, V. A. S. V. Bittencourt, S. V. Kusminskiy, and J. P. Davis, Dynamical backaction magnomechanics, Phys. Rev. X **11**, 031053 (2021).

[40] H. Keshtgar, M. Zareyan, and G. E. Bauer, Acoustic parametric pumping of spin waves, Solid State Commun. **198**, 30 (2014).

[41] B. Flebus, K. Shen, T. Kikkawa, K.-I. Uchida, Z. Qiu, E. Saitoh, R. A. Duine, and G. E. W. Bauer, Magnon-polaron transport in magnetic insulators, Phys. Rev. B **95**, 144420 (2017).

[42] S. Sharma, V. S. V. Bittencourt, and S. Viola Kusminskiy, Protocol for generating an arbitrary quantum state of the magnetization in cavity magnonics, J. Phys. Mater. **5**, 034006 (2022).

[43] J. Graf, S. Sharma, H. Huebl, and S. V. Kusminskiy, Design of an optomagnonic crystal: Towards optimal magnon-photon mode matching at the microscale, Phys. Rev. Res. **3**, 013277 (2021).

[44] F. Engelhardt, V. Bittencourt, H. Huebl, O. Klein, and S. V. Kusminskiy, Optimal broadband frequency conversion via a magnetomechanical transducer, Phys. Rev. Appl. **18**, 044059 (2022).

[45] H. Maier-Flaig, S. Klingler, C. Dubs, O. Surzhenko, R. Gross, M. Weiler, H. Huebl, and S. T. B. Goennenwein, Temperature-dependent magnetic damping of yttrium iron garnet spheres, Phys. Rev. B **95**, 214423 (2017).

[46] C. L. Jermain, S. V. Aradhya, N. D. Reynolds, R. A. Buhrman, J. T. Brangham, M. R. Page, P. C. Hammel, F. Y. Yang, and D. C. Ralph, Increased low-temperature damping in yttrium iron garnet thin films, Phys. Rev. B **95**, 174411 (2017).

[47] E. G. Spencer, R. C. LeCraw, and A. M. Clogston, Low-temperature line-width maximum in yttrium iron garnet, Phys. Rev. Lett. **3**, 32 (1959).

[48] D. Lachance-Quirion, Y. Tabuchi, A. Gloppe, K. Usami, and Y. Nakamura, Hybrid quantum systems based on magnonics, Appl. Phys. Express **12**, 070101 (2019).

[49] J. de Klerk, Behavior of coherent microwave phonons at low temperatures in $Al_2O_3$ using vapor-deposited thin-film piezoelectric transducers, Phys. Rev. **139**, A1635 (1965).

[50] L. Landau and G. Rumer, Absorption of sounds in solids, Phys. Z. Sowjetunion **11**, 18 (1937).

[51] M. Barangi and P. Mazumder, Effect of temperature variations and thermal noise on the static and dynamic behavior of straintronics devices, J. Appl. Phys. **118**, 173902 (2015).

[52] M. Müller, J. Weber, F. Engelhardt, V. A. S. V. Bittencourt, T. Luschmann, M. Cherkasskii, M. Opel, S. T. B. Goennenwein, S. Viola Kusminskiy, S. Geprägs, R. Gross, M. Althammer, and H. Huebl, Chiral phonons and phononic birefringence in ferromagnetic metal–bulk acoustic resonator hybrids, Phys. Rev. B **109**, 024430 (2024).

[53] T. Gilbert, Classics in magnetics: A phenomenological theory of damping in ferromagnetic materials, IEEE Trans. Magn. **40**, 3443 (2004).

[54] Y. Zhao, Q. Song, S.-H. Yang, T. Su, W. Yuan, S. S. P. Parkin, J. Shi, and W. Han, Experimental investigation of temperature-dependent Gilbert damping in Permalloy thin films, Sci. Rep. **6**, 22890 (2016).

[55] M. A. W. Schoen, D. Thonig, M. L. Schneider, T. J. Silva, H. T. Nembach, O. Eriksson, O. Karis, and J. M. Shaw, Ultra-low magnetic damping of a metallic ferromagnet, Nat. Phys. **12**, 839 (2016).

[56] M. A. W. Schoen, J. Lucassen, H. T. Nembach, B. Koopmans, T. J. Silva, C. H. Back, and J. M. Shaw, Magnetic properties in ultrathin 3*d* transition-metal binary alloys. II. Experimental verification of quantitative theories of damping and spin pumping, Phys. Rev. B **95**, 134411 (2017).

[57] M. A. W. Schoen, J. Lucassen, H. T. Nembach, T. J. Silva, B. Koopmans, C. H. Back, and J. M. Shaw, Magnetic properties of ultrathin 3*d* transition-metal binary alloys. I. Spin and orbital moments, anisotropy, and confirmation of Slater-Pauling behavior, Phys. Rev. B **95**, 134410 (2017).

[58] L. Flacke, L. Liensberger, M. Althammer, H. Huebl, S. Geprägs, K. Schultheiss, A. Buzdakov, T. Hula, H. Schultheiss, E. R. J. Edwards, H. T. Nembach, J. M. Shaw, R. Gross, and M. Weiler, High spin-wave propagation length consistent with low damping in a metallic ferromagnet, Appl. Phys. Lett. **115**, 122402 (2019).

[59] E. R. Edwards, H. T. Nembach, and J. M. Shaw, $Co_{25}Fe_{75}$ thin films with ultralow total damping of ferromagnetic resonance, Phys. Rev. Appl. **11**, 054036 (2019).

[60] Y. Chu, P. Kharel, W. H. Renninger, L. D. Burkhart, L. Frunzio, P. T. Rakich, and R. J. Schoelkopf, Quantum acoustics with superconducting qubits, Science **358**, 199 (2017).

[61] $L = 510$ μm, $d = 30$ nm, $v_t = 6.17$ km/s, and $\tilde{v}_t = 3.17$ km/s [72].

[62] D. Polder, On the theory of ferromagnetic resonance, Physica **15**, 253 (1949).

[63] H. T. Nembach, T. J. Silva, J. M. Shaw, M. L. Schneider, M. J. Carey, S. Maat, and J. R. Childress, Perpendicular ferromagnetic resonance measurements of damping and Lande *g*-factor in sputtered $(Co_2Mn)_{1-x}Ge_x$ thin films, Phys. Rev. B **84**, 054424 (2011).

[64] H. Zhang, W. Pang, H. Yu, and E. S. Kim, High-tone bulk acoustic resonators on sapphire, crystal quartz, fused silica, and silicon substrates, J. Appl. Phys. **99**, 124911 (2006).

[65] V. J. Gokhale, B. P. Downey, D. S. Katzer, N. Nepal, A. C. Lang, R. M. Stroud, and D. J. Meyer, Epitaxial bulk acoustic wave resonators as highly coherent multi-phonon sources for quantum acoustodynamics, Nat. Commun. **11**, 2314 (2020).

[66] M. Müller, L. Liensberger, L. Flacke, H. Huebl, A. Kamra, W. Belzig, R. Gross, M. Weiler, and M. Althammer, Temperature-dependent spin transport and current-induced torques in superconductor-ferromagnet heterostructures, Phys. Rev. Lett. **126**, 087201 (2021).

[67] T. S. Suraj, M. Müller, S. Gelder, S. Geprägs, M. Opel, M. Weiler, K. Sethupathi, H. Huebl, R. Gross, M. S. Ramachandra Rao, and M. Althammer, Effect of interfacial oxidation layer in spin pumping experiments on $Ni_{80}Fe_{20}/SrIrO_3$ heterostructures, J. Appl. Phys. **128**, 083903 (2020).

[68] K. Gilmore, Y. U. Idzerda, and M. D. Stiles, Identification of the dominant precession-damping mechanism in Fe, Co,

and Ni by first-principles calculations, Phys. Rev. Lett. **99**, 027204 (2007).

[69] C. Herring, Role of low-energy phonons in thermal conduction, Phys. Rev. **95**, 954 (1954).

[70] P. F. Herskind, A. Dantan, J. P. Marler, M. Albert, and M. Drewsen, Realization of collective strong coupling with ion Coulomb crystals in an optical cavity, Nat. Phys. **5**, 494 (2009).

[71] From Fig. 6 in Appendix B, we find that $g$ is approximately temperature independent, whereas $M_s$ reduces only slightly with increasing temperatures. For the sake of simplicity, we assume a constant $M_s$.

[72] D. Schwienbacher, M. Pernpeintner, L. Liensberger, E. R. J. Edwards, H. T. Nembach, J. M. Shaw, M. Weiler, R. Gross, and H. Huebl, Magnetoelasticity of $Co_{25}Fe_{75}$ thin films, J. Appl. Phys. **126**, 103902 (2019).

[73] X. Zhang, C. L. Zou, L. Jiang, and H. X. Tang, Strongly coupled magnons and cavity microwave photons, Phys. Rev. Lett. **113**, 1 (2014).

[74] G. K. White and M. L. Minges, Thermophysical properties of some key solids: An update, Int. J. Thermophys. **18**, 1269 (1997).

[75] W. E. Tefft, Elastic constants of synthetic single crystal corundum, J. Res. Natl. Bur. Stand. A (USA) **70A**, 277 (1966).

[76] Y.-G. Kim, J.-H. Song, S. Hong, and S.-H. Ahn, Piezoelectric strain sensor with high sensitivity and high stretchability based on kirigami design cutting, npj Flex. Electron. **6**, 52 (2022).

[77] H. Wang, J. Liu, H. Cui, Y. Liu, J. Zhu, H. Wang, G. Song, Z. Li, and D. Chen, Strain sensor with high sensitivity and large response range based on self-assembled elastic-sliding conductive networks, ACS Appl. Electron. Mater. **3**, 1758 (2021).

[78] T. Ueno, J. Qiu, and J. Tani, Self-sensing magnetic force control by composite of giant magnetostrictive and piezoelectric materials, Proc. Int. Conf. Mot. Vibr. Control **6.2**, 1081 (2002).

[79] R. G. Qhobosheane, M. R. P. Elenchezhian, P. P. Das, M. Rahman, M. M. Rabby, V. Vadlamudi, K. Reifsnider, and R. Raihan, Smart self-sensing composite: Piezoelectric and magnetostrictive FEA modeling and experimental characterization using wireless detection systems, Sensors **20**, 6906 (2020).

[80] O. Cugat, J. Delamare, and G. Reyne, Magnetic microactuators and systems (MAGMAS), IEEE Trans. Magn. **39**, 3607 (2003).

[81] G. Reyne, J. Delamare, and O. Cugat, in *Encyclopedia of Materials: Science and Technology* (Elsevier, Amsterdam, 2005), p. 1.